

See discussions, stats, and author profiles for this publication at: <https://www.researchgate.net/publication/235345616>

First-Principles Calculations of Clean and Defected ZnO Surfaces

ARTICLE *in* THE JOURNAL OF PHYSICAL CHEMISTRY C · OCTOBER 2012

Impact Factor: 4.77 · DOI: 10.1021/jp306785z

CITATIONS

11

READS

89

3 AUTHORS, INCLUDING:



Giovanni Cantele

Italian National Research Council

77 PUBLICATIONS 1,444 CITATIONS

SEE PROFILE



Domenico Ninno

University of Naples Federico II

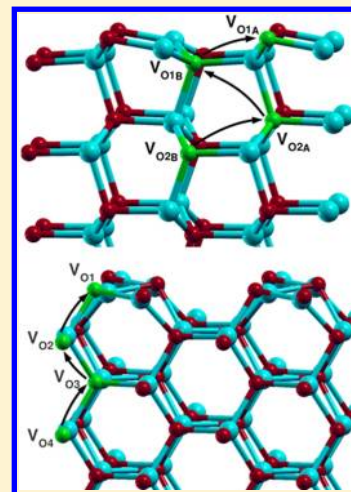
134 PUBLICATIONS 2,269 CITATIONS

SEE PROFILE

First-Principles Calculations of Clean and Defected ZnO Surfaces

Nunzio Roberto D'Amico,^{†,‡} Giovanni Cantele,^{*,†} and Domenico Ninno^{‡,†}[†]CNR-SPIN, Complesso Universitario Monte Sant'Angelo, Dipartimento di Scienze Fisiche, Via Cintia, 80126 Napoli, Italy[‡]Università degli Studi di Napoli "Federico II", Dipartimento di Scienze Fisiche, Complesso Universitario Monte Sant'Angelo, Via Cintia, 80126 Napoli, Italy

ABSTRACT: We report on a theoretical study of the nonpolar ZnO (10 $\bar{1}$ 0) and (11 $\bar{2}$ 0) surfaces carried out in the framework of density functional theory, aiming to elucidate the thermodynamic and kinetic stability of the clean surface against the formation and diffusion of oxygen vacancies. At variance with other oxide materials and ZnO surfaces with different orientation, we show that, under exposure to molecular oxygen in the gas phase, no significant amounts of oxygen vacancies can be sustained by the surface, in agreement with recent Scanning Tunnelling Microscope (STM) observations. However, our calculations show also that under ultrahigh vacuum and high-temperature conditions the observation of oxygen vacancies might be possible, as reported in earlier experiments of Göpel and Lampe.¹ We characterize the defected surfaces electronic and structural properties as a function of the position of the defect with respect to the surface and discuss the diffusion paths of such defects both parallel and across the surface.



■ INTRODUCTION

The detection of specific gas molecules in mixtures of various gases is increasingly required for the control and monitoring of several industrial and medical processes.^{2,3} Solid-state gas sensors based on metal–oxide–semiconductor materials have attracted considerable attention during the past decade^{4–10} due to low cost, small dimensions, and high compatibility with microelectronics processing. The conventional sensing mechanism relies on the charge transfer between the absorbed gas and the metal oxide surface. Depending on the semiconductor type, the charge transfer will either increase or decrease the concentration of the majority carriers, thereby increasing or decreasing the sensor electrical conductance.^{9,10}

Zinc oxide (ZnO), tin dioxide (SnO₂), and titanium dioxide (TiO₂) nanostructures have been identified as promising gas-sensitive materials with many well-documented applications.^{10–16} In particular, ZnO is interesting because of its mixed covalent/ionic character in the chemical bonding, with peculiar properties such as large exciton binding energy (60 meV) and direct band gap (3.4 eV). The versatility and multifunctionality of this material are testified by the wide range of possible applications in varistors,¹⁷ surface acoustic wave devices,¹⁸ transparent conducting oxide electrodes,¹⁹ solar cells,²⁰ blue/UV light emitting devices,²¹ self-powered (nano)-devices,²² and, as mentioned, gas sensors.^{23,24} Of course, it is expected that photocatalysis and gas sensing applications require a precise control of the surface morphology, chemistry, and composition: usually, nanostructures with different surface facets are employed, the (10 $\bar{1}$ 0) and (11 $\bar{2}$ 0) surfaces/facets being the most stable and abundant ones.^{25,26}

Since the ZnO properties are highly sensitive to the nature and concentration of lattice imperfections,^{27,28} understanding the thermodynamics and kinetics of point defects in ZnO is not only of fundamental but also of significant technological interest. For example, zinc migration, which is believed to proceed through the migration of intrinsic defects in the vicinity of grain boundaries—most likely zinc interstitials—has been discussed in connection with the degradation of varistors devices.^{29,30} Moreover, it has been argued that the presence of native surface and subsurface point defects, their concentration, and depth distribution can strongly affect the electronic properties and electrical response of metal–ZnO interfaces and Schottky barriers, as well as the gas adsorption on specific ZnO surfaces.³¹

Some ab initio density functional theory (DFT) calculations have been performed in the past to elucidate the behavior of both intrinsic^{32–35} and extrinsic point defects.^{36,37} It is widely accepted that oxygen vacancies can be considered as the most abundant and the chemically most reactive kind of atomic defects for a large variety of oxides.³⁸ Previous theoretical studies of the bulk ZnO and its surfaces have proven the impact of oxygen deficiency on the electronic and structural properties.^{39–43} Nevertheless, a systematic study of the vacancy diffusion along and across the ZnO nonpolar (10 $\bar{1}$ 0) and (11 $\bar{2}$ 0) surfaces together with the implications on relevant material properties is still lacking. Moreover, the actual

Received: July 9, 2012

Revised: September 12, 2012

Published: September 14, 2012



possibility of observing stable (sub)surface oxygen defects has been experimentally proven in the early 80s^{1,44} but questioned by recent STM experiments.^{45,46}

In this work, we discuss the structural and electronic properties [band structure, density of states (DOS), defect and surface formation energies] of oxygen-deficient surfaces as a function of the defect position with respect to the surface. Oxygen vacancy migration paths are characterized in the framework of the climbing image nudged elastic band method considering the diffusion both parallel and across the surface. The calculated energy barriers and activation temperatures involved in the diffusion process are discussed and compared with the respective bulk counterparts. Moreover, in the case of the (10 $\bar{1}0$) surface, we try to elucidate the apparent disagreement of the available experimental data, which report, depending on the preparation conditions, the observation of a finite concentration of oxygen vacancies or the lack of them close to the surface. With this aim, we also consider the energetics of ZnO-dimer and Zn vacancies, which might occur as the prevailing atomic defects under suitable conditions of temperature and pressure.

■ COMPUTATIONAL DETAILS AND SURFACE MODELS

All first-principles calculations are carried out within the DFT framework as implemented in the QUANTUM ESPRESSO package.⁴⁷ We use the generalized gradient approximation (GGA) parametrized with the Perdew, Burke, and Ernzerhof (PBE) exchange–correlation functional⁴⁸ and Vanderbilt ultrasoft pseudopotentials^{49,50} to mimic the ion cores. The kinetic-energy cutoff for the plane waves is set to 40 Ry and the cutoff for the augmented density to 320 Ry. The crystal/surface geometries are optimized with the direct energy minimization technique of Broyden–Fletcher–Goldfarb–Shanno.⁵¹ The optimization is stopped when each Cartesian component of the force acting on each atom is less than 0.026 eV/Å and the total energy difference between two consecutive steps of the minimization procedure is less than 10^{−4} eV. All the properties presented in the following are referring to the optimized systems.

To test the reliability of the methods and of the pseudopotentials, the bulk ZnO structural and electronic properties have been computed. The ZnO polymorph of interest for the present study is the wurtzite structure, for which the first Brillouin zone (BZ) is sampled using a 16 × 16 × 12 Monkhorst–Pack *k*-point mesh.⁵² The crystallographic parameters are computed from the Birch–Murnaghan equation of state⁵³ and are listed in Table 1, from which a good comparison with the experimental results can be inferred. At variance with the structural properties, the computed band gap (also shown in Table 1) severely underestimates the experimental value, but it is consistent with previous DFT calculations.⁵⁴ While the DFT failure in predicting the band gap is a well-known fact, the underestimation in the case of ZnO goes well beyond the typical errors found for other materials. The road we have followed for curing this problem is that proposed by Janotti and coworkers,⁴⁰ who employ the DFT+*U* scheme. The Hubbard *U* values we included are 12.0 eV on the Zn 3d orbitals and 6.5 eV on the oxygen 2p orbitals, which have already been shown to work well for ZnO.⁵⁴ The lattice parameters, recomputed within the DFT+*U* scheme, change by about 1%, but with a substantial improvement of the electronic properties description (see Table 1). Since only the electronic properties are

Table 1. Lattice Parameters *a* and *c* (in Å), the Internal Coordinate *u*, and the Energy Gap *E*_{gap} (in eV) of Bulk ZnO^a

	<i>a</i>	<i>c</i>	<i>u</i>	<i>E</i> _{gap}
EXP ^{55,56}	3.258	5.220	0.382	3.4
GGA	3.295	5.294	0.381	0.71
GGA+ <i>U</i>	3.258	5.227	0.381	3.31
LDA ⁴⁰	3.195	5.160	0.379	0.80
LDA+ <i>U</i> ⁴⁰	3.148	5.074	0.379	1.51
GGA ⁵⁴	3.289	5.315		0.7
GGA+ <i>U</i> ⁵⁴	3.239	5.257		3.3

^aTheoretical results are obtained from GGA and GGA+*U* calculations. Experimental and theoretical data^{40,54–56} are reported for comparison.

significantly modified using the DFT+*U* scheme, following ref 54 we first optimize the atomic positions at the standard DFT level and only after we include the Hubbard correction for the calculation of the electronic properties.

The ZnO (10 $\bar{1}0$) and (11 $\bar{2}0$) surfaces are modeled using a slab geometry of periodically repeated supercells containing 12 atomic planes.⁵⁷ A vacuum width of 15 Å separates each slab from its periodic images to avoid spurious interactions between repeated slabs. As evidenced by Figure 1, the [10 $\bar{1}0$] direction

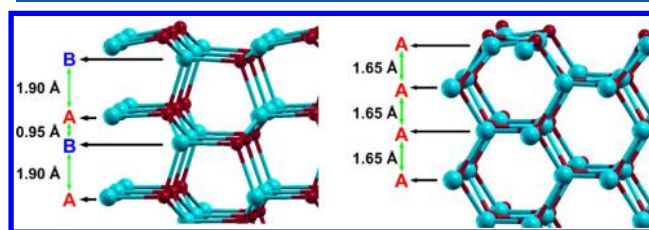


Figure 1. Side view of the reconstructed ZnO (10 $\bar{1}0$) and (11 $\bar{2}0$) stoichiometric surfaces (left and right panel, respectively). Oxygen atoms are small red, and zinc atoms are large blue. The lattice plane distances reported on the left are those of the bulk crystal.

can be defined as consisting, in the bulk crystal geometry, of an ABABAB... stacking of ZnO planes, in which each B plane has a distance of 0.95 and 1.90 Å from the two nearest A planes. Therefore, we can identify two potentially stable, stoichiometric [10 $\bar{1}0$] surface terminations, but only results concerning the A plane termination will be presented here since it has been shown that it is the most stable one.⁵⁸ On the other hand, the [11 $\bar{2}0$] direction can be viewed as a stacking of equidistant lattice planes; therefore, only one possible surface termination can be identified, with two Zn–O dimers in the unit cell.

For both surfaces, we adopt an “asymmetric” slab model, with the atoms in the four bottom atomic planes anchored to their bulk positions. All the other atoms are allowed to fully relax according to their interatomic forces. The surface and the point defect(s) are thus modeled only on the top side of the slab. It has already been shown that modeling the surface in this way leads to a much better convergence of the structural and electronic properties with respect to the number of layers in the slab.⁵⁹ A dipole correction has been applied to get rid of spurious electric fields across the slab, arising from the combination of periodic boundary conditions with the asymmetric slab model.⁶⁰

Isolated oxygen vacancies in bulk ZnO have been modeled by removing a single oxygen atom from a 3 × 3 × 2 supercell (the BZ sampling is performed using a 5 × 5 × 6 *k*-point grid),

while for the study of oxygen vacancies at the ZnO (10 $\bar{1}$ 0) and ZnO (11 $\bar{2}$ 0) surfaces, we have considered, respectively, 2×2 and 2×1 surface supercells to study the dependence of the calculated properties as a function of the defect depth with respect to the surface. These supercells correspond to a minimum vacancy–vacancy distance of 9.8, 6.6, and 5.3 Å for the defected bulk, (10 $\bar{1}$ 0), and (11 $\bar{2}$ 0) ZnO surfaces, respectively. Convergence tests with respect to the vacancy–vacancy distance showed small variations (within 0.1 eV) of the vacancy formation energies and of the surface band gap. Yet, electronic levels localized around the defect did show a larger sensitivity to the vacancy concentration. As such, defected surface band structure calculations were performed using a 3×3 supercell.

To shed light on the stability of the above-mentioned defected surface and bulk ZnO models, we have carried out an extensive thermodynamic and kinetic analysis, aimed to identify the most favorable configurations as well as migration paths for oxygen vacancies in thermally activated diffusion processes. According to a well-established methodology,^{61–64} the relative stability (against oxidation and reduction processes) of different (defected or undefected) surfaces in equilibrium with an oxygen atmosphere at a given pressure p and temperature T is found by calculating the surface formation energy (per unit area) defined as

$$\sigma(T, p) = \frac{1}{A} \left[E_{\text{slab}} - N_{\text{Zn}} E_{\text{ZnO}}^{\text{bulk}} + N_{\text{vac}} \frac{E_{\text{O}_2}}{2} + N_{\text{vac}} \Delta\mu_{\text{O}}(T, p) \right] - \frac{1}{2A} [E_{\text{slab}}^0 - N_{\text{Zn}} E_{\text{ZnO}}^{\text{bulk}}] \quad (1)$$

where E_{slab} is the total energy of the slab under investigation; N_{Zn} and N_{vac} are the number of Zn atoms and oxygen vacancies in the slab supercell; A is the surface supercell area; $E_{\text{ZnO}}^{\text{bulk}}$ is the energy of bulk ZnO per formula unit; E_{slab}^0 is the energy of the stoichiometric slab with the atoms fixed at their ideal bulk positions; E_{O_2} is the total energy of the spin-polarized O₂ molecule; and $\Delta\mu_{\text{O}}(T, p)$ is the variation, at given pressure and temperature, of the oxygen chemical potential.

The term $(1/2A)[E_{\text{slab}}^0 - N_{\text{Zn}} E_{\text{ZnO}}^{\text{bulk}}]$ in eq 1 is the surface formation energy of a stoichiometric slab with the atoms fixed at their bulk positions. It must be subtracted to get rid of the contribution of the “unrelaxed” side of the slab to the formation energy, as a consequence of the asymmetric supercell model we have adopted.

Equation 1 is simply derived by taking into account that experimentally the chemical potentials of the O and Zn atoms cannot be varied without bounds. Indeed, the O and Zn atoms are assumed to form no condensate on the surface. Consequently, the chemical potential of each species must be lower than the Gibbs free energy of an atom in the stable phase of the considered species (assumed to be the *hcp* Zn bulk metal and the O₂ molecule in the gas phase, respectively). Moreover, if there is enough bulk material to act as a thermodynamic reservoir, the chemical potentials of O and Zn are not independent but related by the Gibbs free energy of the bulk oxide: $\mu_{\text{Zn}}(T, p) + \mu_{\text{O}}(T, p) = g_{\text{ZnO}}^{\text{bulk}}(T, p)$ where $g_{\text{ZnO}}^{\text{bulk}}(T, p)$ is the Gibbs free energy of bulk ZnO per formula unit. It is also worth pointing out that, in principle, eq 1 should contain the Gibbs free energies of the system, rather than the DFT total energies. Nevertheless, it has been argued that the vibrational

contribution to the Gibbs free energy either can be neglected with respect to the other contributions or does not significantly affect the physical conclusions,⁶⁴ even though in special situations such approximations might not be valid. From eq 1 we observe that $\sigma(T, p)$ is a function of only $\Delta\mu_{\text{O}}(T, p)$ whose temperature and pressure dependence is defined by

$$\Delta\mu_{\text{O}}(T, p) = \Delta\mu_{\text{O}}(T, p^0) + \frac{1}{2} k_{\text{B}} T \ln \left(\frac{p}{p^0} \right) \quad (2)$$

where $p^0 = 1$ atm. The temperature dependence of $\Delta\mu_{\text{O}}(T, p^0)$ includes contributions from molecular vibration and rotations, as well as ideal-gas entropy at 1 atm pressure. These data can be found in thermodynamic tables.⁶⁵ By employing eq 2, one can provide the diagrams of the thermodynamic stability with a clear physical meaning behind the calculated curves.

For all stoichiometric and defected slabs, formation energy calculations are performed at the DFT level of the theory. Indeed, a complication arises when total DFT+ U energies are used in calculations involving energy differences because of the need of calculating elemental reference energies, e.g., metallic bulk Zn and O₂ molecule in our case. On one hand, the appropriate U value for the Zn *d* states should be smaller in the metal than in ZnO, due to the difference in screening. On the other hand, total energies should in practice be compared only for the same U .^{66,67} Thus, the DFT+ U vacancy formation energies might not be accurate, if different values of U are taken for the semiconductor and the metal.

According to the transition state theory,⁶⁸ the kinetics underlying the thermally activated process of vacancy diffusion is governed by the energy barrier E_{b} to be overcome for the vacancy to jump from one site to a neighbor one. The calculation of E_{b} is performed by employing the climbing image nudged elastic band method,⁶⁹ aimed to find the minimum energy path (MEP) connecting an initial and a final state configuration corresponding to two minima of the potential energy surface. An accurate sampling of the MEP is performed using 11 intermediate images (between the initial and final point of the path). Forces along the MEP were minimized to less than 0.1 eV/Å to ensure convergence. Once E_{b} is known, the process rate is easily defined as $\Gamma = \Gamma_0 \exp(-(E_{\text{b}}/k_{\text{B}}T))$, where the prefactor Γ_0 is the ratio of the vibrational frequencies at the initial configuration to the frequencies at the saddle point; k_{B} is the Boltzmann constant; and T is the temperature. A reasonable estimate of the temperature at which the oxygen vacancy becomes mobile can be obtained by taking the usual definition of the activation temperature, i.e., the temperature at which the jump rate Γ is 1 s^{−1}. To a good approximation Γ_0 can be taken as a typical phonon frequency, i.e., 10¹³ s^{−1}. Therefore, we can use $\Gamma = 1$ s^{−1}, $\Gamma_0 = 10^{13}$ s^{−1}, and the calculated E_{b} values for each path to estimate the annealing temperature (this typically slightly overestimates the temperature at which oxygen vacancies become mobile).

As a final remark, it is worth mentioning that careful tests have been performed to ensure full convergence of the main computed properties (formation energies, energy barriers in diffusion paths, etc.) with respect to the parameters entering the calculations (cutoff, BZ sampling, etc.).

RESULTS AND DISCUSSION

Clean ZnO (10 $\bar{1}$ 0) and ZnO (11 $\bar{2}$ 0) Surfaces. The nonpolar ZnO (10 $\bar{1}$ 0) and (11 $\bar{2}$ 0) surfaces are obtained by cutting the bulk crystal along planes parallel to the *c* axis. The

respective surface geometries are sketched in Figure 1. While in the bulk Zn and O atoms are 4-fold coordinated, on the (10 $\bar{1}$ 0) and (11 $\bar{2}$ 0) surfaces they become 3-fold coordinated. The resulting reconstruction keeps limited to surface atoms. For example, for the (10 $\bar{1}$ 0) surface the surface Zn and the uppermost O atoms relax inward by 0.341 and 0.003 Å, respectively (to be compared with the LEED experimental outcomes⁷⁰ of 0.3 ± 0.15 Å and 0.1 ± 0.05 Å). On the other hand, only a slight reduction of the Zn–O bond length (from 2.02 to 2.01 Å) on the subsurface layer is observed. The surface relaxation leads to a shortening of Zn–O bonds (from 2.02 to ~ 1.9 Å) and to a tilt of the Zn–O dimers by 10.3° and 7.7° for the (10 $\bar{1}$ 0) and (11 $\bar{2}$ 0) surfaces, respectively. This relatively small tilt angle, together with the Zn–O bond length contraction of about 7%, is a signature of the mixed character of the chemical bond which turns out to be highly ionic but with a significant covalent contribution.

The surface formation energies per unit area obtained from eq 1 with $N_{\text{vac}} = 0$ are 0.052 and 0.055 eV/Å² for the (10 $\bar{1}$ 0) and (11 $\bar{2}$ 0) surfaces, respectively. The (slightly) lower stability of the latter can be ascribed to its rougher morphology (when compared with the (10 $\bar{1}$ 0) surface) and agrees with experimental STM results.^{45,71} Our results are compatible with the calculations of Meyer and Marx⁷² that use a symmetric slab model. However, a discrepancy is found with the results of Spencer et al.⁷³ These authors use an asymmetric slab model with fixed bottom layers (the same strategy as ours) but do not subtract, as we do in eq 1, the contribution coming from the unrelaxed side, thus reporting the slab cleavage energy (with contributions coming from both the relaxed and the unrelaxed sides of the slab).

Electronic band structure calculations, performed within the GGA+U, give a direct band gap for both surfaces. As a technical remark, we point out that, because we use an asymmetric slab model, some spurious intragap surface states show up that are associated with the bulk-like side of the slab. For this reason, both the surface band structure and the total DOS have been obtained by retaining the only contributions coming from electronic states with a significant projection (>0.2) onto the atomic orbitals associated to the layers that have been optimized during the calculations. When compared with the bulk value (3.31 eV), the band gap gets reduced (3.17 eV) for the (10 $\bar{1}$ 0) surface, whereas a larger value (3.47 eV) is obtained for the (11 $\bar{2}$ 0) surface. The character of the near-gap states can be inferred from the analysis of the projected DOS (PDOS) on atomic orbitals, shown in Figure 2. For both the (10 $\bar{1}$ 0) and (11 $\bar{2}$ 0) surfaces, the top valence band is mainly derived from the p orbitals of O atoms with Zn atoms giving negligible contribution. On the other hand, the bottom conduction band is strongly dominated by the bulk contributions as seen in the figure insets. These results are in agreement with recent first-principles studies.⁷⁴

Oxygen-Deficient Surfaces. We now have all the basic elements for discussing the effects due to oxygen vacancy. As far as the structural properties are concerned, the presence of a vacancy in the topmost layer induces an inward displacement of the unpaired Zn atom so as to restore a bulk-like 4-fold coordination with the two neighbor Zn atoms of the second layer, in agreement with previous theoretical studies.^{58,75–77} Significant relaxation effects are also observed when the vacancy is located in the first two subsurface layers. For deeper vacancies, relaxation effects are more moderate and very similar to those observed in the defected bulk crystal. Moreover, the

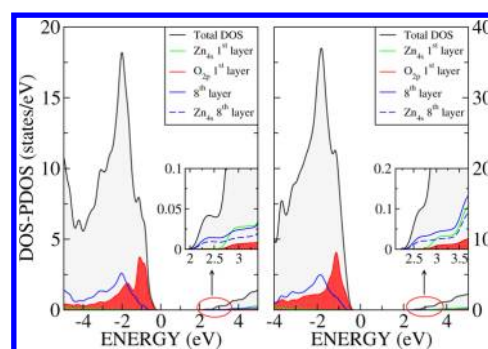


Figure 2. PDOS in the near-gap region for the (10 $\bar{1}$ 0) and (11 $\bar{2}$ 0) surfaces (left and right panel, respectively). The insets show a zoom in proximity of the conduction band edge. The projections are made on: (i) surface atomic orbitals (Zn 4s and O 2p states) and (ii) atomic orbitals belonging to a bulk-like layer (we choose the eighth layer and project onto either all the atomic orbitals or only Zn 4s states belonging to it). This allows us to distinguish between “surface” and “bulk” contributions as well as between O and Zn atomic orbital contributions.

vacancy-induced distortions are mostly localized around the defect, whereas the geometry of the stoichiometric system is almost preserved in the regions far from the defect site.

A key issue in the applications of such surfaces in more complex systems, such as gas sensors and ZnO contacts, is given by the defect concentration and depth distribution (for example, such factors have been shown to play a role in the electronic processes occurring at ZnO Schottky barriers³¹). To get insight into this point, the vacancy formation energy, which measures the energy required to remove an oxygen atom from the stoichiometric surface, has been calculated as a function of the vacancy position with respect to the surface. This energy is defined as

$$E_{\text{vf}} = E_{\text{slab}} + N_{\text{vac}} \times \frac{1}{2} E_{\text{O}_2} - E_{\text{slab}}^{\text{st}} \quad (3)$$

where E_{slab} and $E_{\text{slab}}^{\text{st}}$ are the DFT total energies of the slab containing the defect(s) and of the stoichiometric slab, respectively. The computed values of E_{vf} as a function of the oxygen vacancy position and for a defect concentration of 25% are plotted in Figure 3(a). The surface vacancy corresponds to 0 Å depth and has the lowest formation energy (2.84 and 2.72 eV for the (10 $\bar{1}$ 0) and (11 $\bar{2}$ 0) surfaces, respectively). Higher formation energies are obtained for deeper positions of the vacancy (for example, 3.32 and 3.37 eV for subsurface vacancies in the (10 $\bar{1}$ 0) and (11 $\bar{2}$ 0) surface, respectively), monotonically approaching the bulk limit of 3.64 eV for sufficiently deep sites (even in the case of the (10 $\bar{1}$ 0) surface in which, as previously mentioned, an A–B stacking of the atomic planes can be identified).

In Figure 4a and Figure 4b, we show the band structure (calculated using the GGA+U approach) of the ZnO (10 $\bar{1}$ 0) and (11 $\bar{2}$ 0) surfaces in the presence of a single oxygen vacancy in the supercell (with a concentration of 11% and 12%, respectively). The presence of the defect is responsible for the appearance of an occupied dispersionless band which is located about 2 eV above the bulk crystal top valence band. Such a band, as revealed by the PDOS analysis, is mainly derived from the Zn_{4s} atomic orbitals belonging to the atoms surrounding the vacancy, with a smaller contribution coming from O_{2p} orbitals of the atoms closest to the vacancy itself. This is confirmed by the electron charge density distribution of the

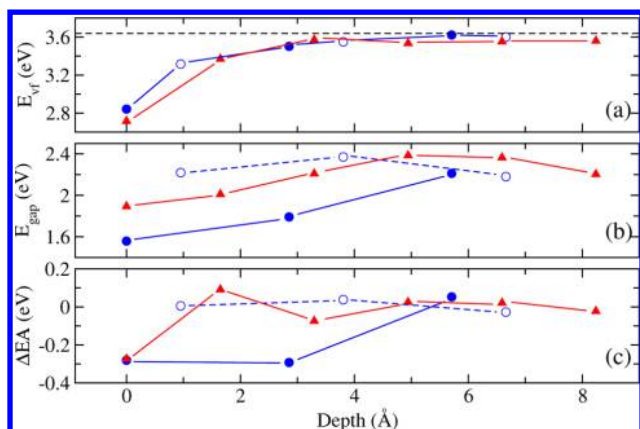


Figure 3. (a) Vacancy formation energy E_{vf} , (b) energy gap E_{gap} , and (c) electron affinity variation with respect to the stoichiometric surface (ΔEA) as a function of the defect depth in the slab. The origin on the abscissa is at the position of the surface vacancy. Circles and triangles distinguish the two different surface orientations ((10 $\bar{1}$ 0) and (11 $\bar{2}$ 0), respectively), while full or empty circles distinguish, for the (10 $\bar{1}$ 0) slab, the vacancy in the A or B planes, respectively. The black dotted line corresponds to the formation energy of a bulk oxygen vacancy. The defect concentration is 25% (larger unit cells, corresponding to 11% and 12% defect concentration for the two surfaces, respectively, give rise to E_{vf} and ΔEA variations by only 0.1 eV).

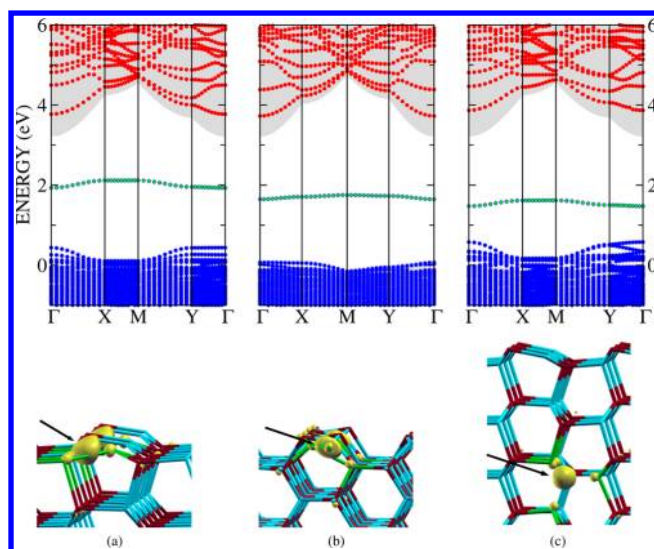


Figure 4. Band structures calculated within the GGA+U approach (top panels) and contour plots of the square modulus of the defect band wave function (at Γ point) (bottom panels) for (a) the ZnO (10 $\bar{1}$ 0) surface with an oxygen vacancy in the surface layer, (b) the ZnO (11 $\bar{2}$ 0) surface with an oxygen vacancy in the surface layer, and (c) the ZnO (10 $\bar{1}$ 0) surface with an oxygen vacancy in the sixth layer. The vacancy concentration is 11% in (a) and (c) and 12% in (b). Occupied (unoccupied) bands are reported as blue (red) filled circles. The green square symbols identify the electronic levels with a significant projection (>0.4) on the atomic orbitals of the Zn atoms surrounding the vacancy. The shaded regions correspond to the bulk band structure projected onto the surface two-dimensional BZ. The energy zero is set to the top bulk valence band. In all cases the almost flat band around ~ 2 eV corresponds to a defect electronic level. The contours correspond to a density equal to 15% of the maximum value, and the arrows mark the defect position.

defect states. The contour plot of the square modulus of the defect band wave function (calculated at Γ point), reported in

the bottom panels of the same figure, clearly shows a localized character, with the majority of the wave function around the defect site. A qualitatively similar behavior is found when the defect occupies deeper positions. As an example, we show in Figure 4c the band structure of the (10 $\bar{1}$ 0) surface with a single vacancy in the sixth atomic layer (11% vacancy concentration). As with the surface vacancy, a defect level appears within the bulk band gap. The only significant difference is a downward shift of the defect band as the vacancy approaches bulk-like positions. Moreover, as revealed by the bottom panel of the same figure, the localized character of the defect-related electronic levels gets more pronounced.

The calculated energy gap E_{gap} as a function of the vacancy depth is reported in Figure 3b. E_{gap} is strongly influenced by the hybridization of the atomic orbitals surrounding the vacancy, which explains its dependence on the vacancy site. In particular, a moderate dependence on the depth is found for O vacancies in the B planes of the (10 $\bar{1}$ 0) surface, whereas a more significant dependence is found when the vacancy is located within the A planes of the (10 $\bar{1}$ 0) surface or for the (11 $\bar{2}$ 0) surface. This is a signature of how the atomic relaxation around the point defect is not the same for all the investigated systems, leading to different positions of the lowest occupied and highest unoccupied electronic levels.

We have also investigated the electron affinity (EA) variations with respect to the stoichiometric surfaces (ΔEA) induced by the presence of the O vacancies [see Figure 3c]. The electron affinity can be easily calculated once the vacuum level has been determined from the self-consistent electrostatic potential.⁷⁸ The results for the stoichiometric ZnO (10 $\bar{1}$ 0) and (11 $\bar{2}$ 0) surfaces are 5.34 and 5.49 eV, respectively. It is seen from Figure 3(c) that only surface and, to a smaller extent, subsurface oxygen vacancies can induce changes of the EA. In particular, we observe considerable EA variation (-0.28 eV and -0.27 eV for the (10 $\bar{1}$ 0) and (11 $\bar{2}$ 0) surfaces, respectively) in the presence of surface vacancies. O vacancies in the B planes of the (10 $\bar{1}$ 0) surface produce only small EA variations. Moreover, it can be noticed that the presence of an oxygen vacancy in the A plane of (10 $\bar{1}$ 0) surface at a depth of 2.85 Å induces EA changes as large as -0.29 eV. As with the energy gap, the EA variations bring the signature of different atomic rearrangement around the point defect as a function of its depth.

As a last point of this section, we want to compare the stability of the investigated surfaces under experimental conditions. With this aim, we consider surfaces with different vacancy concentrations, assumed to be in equilibrium with an external environment (molecular oxygen in the gas phase). The quantity to be computed is the surface formation energy per unit area, eq 1, which, at variance with the stoichiometric surface, depends on $\Delta\mu_{\text{O}}(T, p)$ which is a function of temperature and pressure [eq 2]. The lower bound for $\Delta\mu_{\text{O}}(T, p)$ is given by the formation energy of the bulk ZnO crystal E_f^{ZnO} (referred to as the bulk Zn crystal and molecular oxygen in the gas phase). We estimate $E_f^{\text{ZnO}} = -2.80$ eV, in agreement with previous theoretical calculations.^{34,79} The given estimation of $E_f^{\text{ZnO}} = -2.80$ eV does not match the experimental value (-3.63 eV, measured⁶⁵ at $T = 298$ K and $p = 1$ bar). The discrepancy arises from using the DFT total energy of the O₂ molecule, which is well-known to be severely underestimated in DFT-PBE. Another possible route, pursued in the literature, is that the total energy of the O₂ molecule is chosen in such a way that, combined with the DFT-PBE total energies of bulk metallic Zn and bulk ZnO, the experimental

value of E_f^{ZnO} is correctly predicted.^{42,80} In this case, because the formation energy of an O vacancy becomes larger but the range of allowed chemical potentials (horizontal axis in Figure 5) is

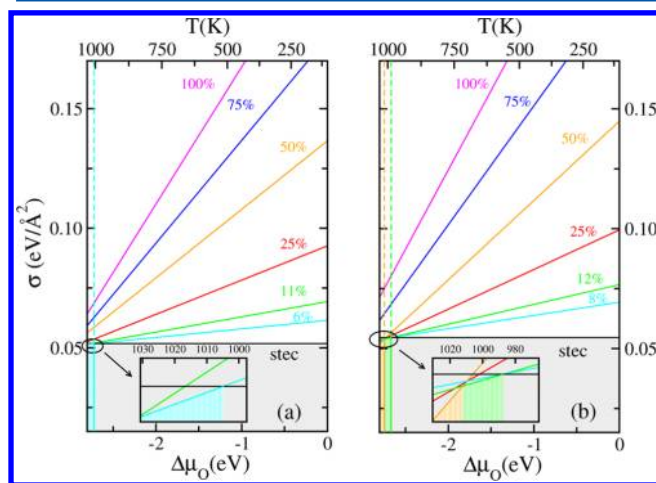


Figure 5. Surface free energies for the nonpolar ZnO (10 $\bar{1}0$) [left panel] and (11 $\bar{2}0$) [right panel] surfaces as a function of the oxygen chemical potential. Different surface vacancy concentrations are considered. The top axis shows, according to eq 2, the conversion of the chemical potential range to temperature for an oxygen gas partial pressure of $\sim 10^{-10}$ atm. The insets show a magnification of the temperature range where the defective surface is thermodynamically more stable than the defect-free surface.

wider, the same (qualitative) results for surface stabilities are obtained because all the thermodynamic plots are shifted toward high temperatures. In Figure 5 we show the surface formation energy per unit surface area of stoichiometric and defected surfaces as a function of $\Delta\mu_O(T, p)$ for several reduction percentages. Only surface defects are considered. The top horizontal axis reports, according to eq 2, the conversion scale of the chemical potential (bottom horizontal axis) to temperature, for an oxygen partial pressure of 10^{-10} atm. The results show that, at variance with other oxide materials and other ZnO surface terminations, the stoichiometric surface is thermodynamically the most stable over most of the temperature range.⁸¹ Only for sufficiently low vacancy concentrations, ultrahigh vacuum conditions, and high temperature (~ 1000 K in Figure 5), the defected system can become more stable. While these pressure/temperature conditions under which defects are stable might be considered too severe, it should be noticed that under similar conditions Göpel and Lampe^{1,44} were able to obtain thermodynamically stable ZnO (10 $\bar{1}0$) surfaces in the presence of oxygen vacancies. In particular, intrinsic point defects were intentionally induced, with a maximum coverage of 10^{-2} , by pursuing several routes, including: (i) high-temperature treatment and subsequent cooling under ultrahigh vacuum conditions, (ii) UV illumination, leading to thermally activated desorption of oxygen atoms, (iii) in the absence of UV light, by CO exposure and subsequent CO₂ desorption. Of course, the surface defects could only be frozen in the absence of O₂ since they react rapidly with oxygen even at low temperature ($T \leq 700$ K). In the same experiment, fundamental effects induced by the presence of oxygen vacancies, such as the formation of strong accumulation layers, surface free carriers, and variations in rates of charge transfer, were extensively characterized.

It should be pointed out that more recent studies, based on atomically resolved STM experiments,^{45,46} have found no signature of the presence of oxygen defects on the same surface. As far as we can understand, the different conclusions might originate from different preparation conditions. In other words, while it is not likely to find significant concentrations of defects on the surfaces under investigation under “ordinary” temperature and pressure conditions, it is possible to intentionally induce such defects if suitable preparation conditions are met.

A last question concerns the possibility of observing other kind of defects, such as a missing ZnO dimer or a Zn vacancy. Such a possibility has been theoretically argued for⁴² and has been given some evidence by recent experiments.⁴⁶ To get more insight, in Figure 6 we compare, for the (10 $\bar{1}0$) surface (3

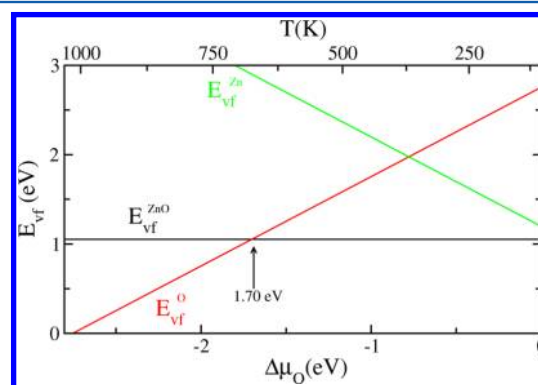


Figure 6. Formation energy of a ZnO dimer (black line), a Zn vacancy (green line), and an O vacancy (red line) on the ZnO (10 $\bar{1}0$) as a function of the oxygen chemical potential. All the energies are referred to the stoichiometric, clean surface. As with eq 3, which defines the O vacancy formation energy, we define the formation energy of a single ZnO dimer and a Zn vacancy, respectively, as $E_{\text{vf}}^{\text{ZnO}} = E_{\text{slab}} + E_{\text{ZnO}}^{\text{bulk}} - E_{\text{slab}}^{\text{st}}$ and $E_{\text{vf}}^{\text{Zn}} = E_{\text{slab}} + E_{\text{Zn}}^{\text{bulk}} - (1/2)E_{\text{O}_2} - E_{\text{slab}}^{\text{st}}$. The top horizontal axis reports, according to eq 2, the conversion scale of the chemical potential (bottom horizontal axis) to temperature, for an oxygen partial pressure of 10^{-10} atm.

$\times 3$ unit cell), the defect formation energy (with respect to the stoichiometric surface) of a surface oxygen vacancy, Zn vacancy, and ZnO vacancy as a function of the oxygen chemical potential. The $E_{\text{vf}} = 0$ axis corresponds to the stoichiometric surface. The results show that while, as previously discussed, extremely reducing conditions are needed for the defected surface to become more stable the same condition cannot be met in the presence of the Zn or ZnO vacancies. Moreover, at sufficiently high temperatures (~ 700 K in the shown example), the O vacancy is the most stable defect, in agreement with previous results.⁴² Finally, it should be noticed that, within the approximation of the present calculations, even strongly oxidizing conditions are not enough for the Zn vacancy to be more stable than either the other defects or the stoichiometric system.⁸²

Diffusion Mechanisms of O Vacancy. The diffusion mechanism of oxygen and zinc vacancies in the bulk ZnO crystal is technologically important, and it has been extensively investigated.^{39–41,83,84} On the other hand, the diffusion of oxygen vacancies in proximity of ZnO surfaces has been less investigated.⁸⁵ The results of the previous sections allow us to conclude that the formation of vacancies on the ZnO surfaces of interest for the present work is likely only under quite stringent experimental conditions. This implies that a vacancy

in proximity of the surface will immediately recombine with ambient oxygen under ordinary conditions. Nevertheless, it is legitimate to wonder what happens to a defect which has been created in deeper positions. The magnitude of the diffusion barriers might induce defect migration (and successive recombination) of the defect toward the surface or prevent such a mechanism. In particular, it is relevant to point out possible differences arising in the diffusion pathways within planes parallel to the surface or along the direction orthogonal to it.

As far as the oxygen vacancy diffusion in the bulk crystal is concerned, we have considered only the paths connecting first neighbor oxygen sites because they correspond to the lowest energy barriers. Among the possible vacancy jumps, there are six symmetric equivalent paths parallel to the (0001) plane and six equivalent paths with components parallel to the [0001] axis. For an ideal *hcp* lattice ($c/a = (8/3)^{1/2} = 1.633$) all these paths are equivalent, but in the ZnO they are different because the axial ratio of the oxygen *hcp* sublattice is slightly smaller than the ideal one ($c/a = 1.606$). Therefore, the two above-mentioned sets of paths will be referred to as in-plane (IN) and out-of-plane (OUT), respectively.

The calculated diffusion pathways are shown in Figure 7, while the diffusion barriers and the estimated annealing

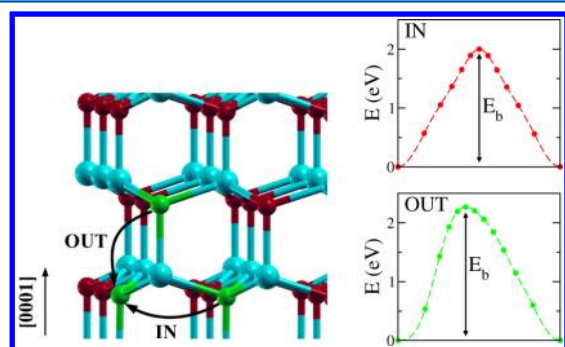


Figure 7. Schematic illustration (left panel) of diffusion paths (right panels) for oxygen vacancies in the wurtzite lattice. IN and OUT denote, respectively, the in-plane diffusion path within the (0001) plane and out-of-plane diffusion with component parallel to the [0001] axis. Only vacancy hopping between first-neighbor oxygen sites is investigated. The green spheres represent the oxygen sites involved in the two diffusion paths, whereas the blue (red) spheres represent the other zinc (oxygen) atoms.

temperatures are reported in Table 2. A $2 \times 2 \times 2$ BZ sampling has been employed in these calculations to reduce the computational cost (we have verified that a better BZ sampling produces no significant changes in the computed paths). The OUT path shows a higher barrier, of about 0.3 eV, than the IN path. Such small anisotropies in the migration barriers are

Table 2. Calculated Migration Barrier E_b and Estimated Annealing Temperature T_a for the Oxygen Vacancy Hopping between First Neighbor Sites in the Bulk ZnO Crystal^a

	this work		ref 39	ref 40	ref 41
	E_b (eV)	T_a (K)	E_b (eV)	E_b (eV)	E_b (eV)
IN	2.00	775	1.87	2.36	2.06
OUT	2.27	880	2.55	2.36	2.34

^aPrevious literature results are also reported for comparison.

expected since, as pointed out, the local geometry around the oxygen vacancy has an almost, but not full, tetrahedral symmetry. From Table 2 we can see that the oxygen vacancies become mobile only at high temperature, in agreement with the experimental findings⁸⁶ showing that oxygen vacancies are stable up to ~ 670 K. In Table 2 we also show previous theoretical calculations of the diffusion barriers. While our results agree with those reported in ref 41, it can be noticed that Erhart and Albe³⁹ find differences as large as 0.7 eV between migration barriers along the IN and OUT pathways. As already suggested by Janotti and Van de Walle,⁴⁰ we have verified (by directly reproducing the calculation) that the discrepancy arises from the small supercell (32 atoms) used in ref 39, which does not guarantee full convergence of the calculated barriers.

Due to computational issues, for the vacancy diffusion in proximity of the (10 $\bar{1}$ 0) and (11 $\bar{2}$ 0) surfaces, we have used an 8 atomic layer model with the atoms in the two bottom layers anchored to their bulk positions. No significant changes in the calculated energy barriers have been observed in test cases where a 12 atomic layer slab model has been employed. 4×3 and 2×4 *k*-point meshes have been used to sample the two-dimensional BZ of the ZnO (10 $\bar{1}$ 0) and (11 $\bar{2}$ 0) surface supercells, respectively.

We consider different oxygen sites within the slab as possible hopping centers (see Figure 8), to bring out differences between migration processes occurring either within a given atomic layer or across different atomic layers. We report the barriers along the most favorable pathways together with the estimated annealing temperatures in Table 3 and Table 4 for the (10 $\bar{1}$ 0) and (11 $\bar{2}$ 0) surfaces, respectively. Direct and inverse barriers refer to asymmetric paths, connecting local minima with different energies. The results show that, for both surfaces, the most favored diffusion process occurs within the surface layer (with a migration barrier of about 1.2 eV). On the other hand, in-plane (namely, parallel to the surface) diffusion processes within the subsurface layers are much more unlikely, being driven by energy barriers as large as 1.7–2.0 eV (see the $V_{O1B} \rightarrow V_{O1B'}$, $V_{O2A} \rightarrow V_{O2A'}$, $V_{O2B} \rightarrow V_{O2B'}$ and $V_{O2} \rightarrow V_{O2'}$, $V_{O3} \rightarrow V_{O3'}$, $V_{O4} \rightarrow V_{O4'}$ paths in Table 3 and Table 4, respectively). Interestingly, the in-plane diffusion barrier is not a monotonic function of the depth. This is shown in Figure 9, where the variation of E_b as a function of the atomic layer depth is plotted. It can be easily argued that the considered diffusion paths for the (10 $\bar{1}$ 0) and (11 $\bar{2}$ 0) surfaces would correspond to the previously discussed IN and OUT paths in the bulk crystal, respectively. For this reason, the two panels of Figure 9 show different bulk limits (see Table 2), which are approached as the atomic layer depth increases.

As far as out-of-plane (namely, across different atomic layers) migration processes are concerned, we observe that the diffusion from the surface to the subsurface ($V_{O1A} \rightarrow V_{O1B'}$, $V_{O1A} \rightarrow V_{O2A'}$, $V_{O1} \rightarrow V_{O2'}$, and $V_{O1} \rightarrow V_{O3}$ paths) appears to be largely inhibited ($E_b \sim 2.0$ eV). Smaller barriers are found for the inverse process (subsurface to surface diffusion) with the $V_{O2A} \rightarrow V_{O1A}$ process showing a barrier (~ 1.2 eV) comparable with the surface, in-plane diffusion barrier. Therefore, we can conclude that the most likely migration processes correspond to the vacancy hopping in the surface layer (with typical activation temperature less than 500 K).

To conclude this section, we show in Figure 10 the calculated potential energy profile and selected NEB images for the $V_{O1} \rightarrow V_{O1}$ in-plane diffusion pathway of an oxygen vacancy parallel

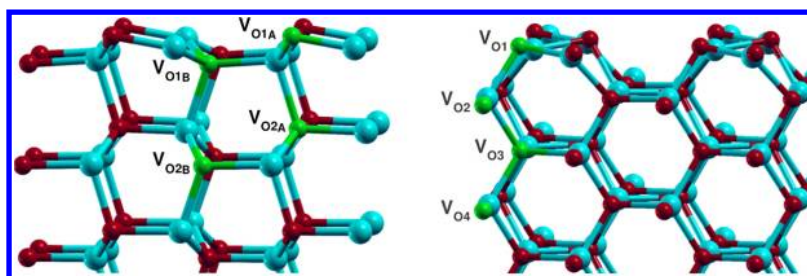


Figure 8. Oxygen vacancy sites (highlighted in green) considered as possible hopping sites in the vacancy diffusion process. The migration paths of Table 3 and Table 4 connect pairs of these sites. Left and right panels are for the (10 $\bar{1}$ 0) and (11 $\bar{2}$ 0) surfaces, respectively.

Table 3. Calculated Migration Barrier E_b and Estimated Annealing Temperature T_a for the Vacancy Diffusion Process Across the (10 $\bar{1}$ 0) ZnO Surface^a

	E_b (eV)		T_a (K)	
	direct	inverse	direct	inverse
$V_{O1A} \rightarrow V_{O1A}$	1.265	1.265	490	490
$V_{O1B} \rightarrow V_{O1B}$	1.721	1.721	667	667
$V_{O2A} \rightarrow V_{O2A}$	1.416	1.416	549	549
$V_{O2B} \rightarrow V_{O2B}$	1.955	1.955	757	757
$V_{O1A} \rightarrow V_{O1B}$	2.099	1.639	814	635
$V_{O1A} \rightarrow V_{O2A}$	1.901	1.240	737	481

^aThe oxygen vacancy sites are defined in Figure 8, left panel.

Table 4. Calculated Migration Barrier E_b and Estimated Annealing Temperature T_a for the Vacancy Diffusion Process Across the (11 $\bar{2}$ 0) ZnO Surface^a

	E_b (eV)		T_a (K)	
	direct	inverse	direct	inverse
$V_{O1} \rightarrow V_{O1}$	1.224	1.224	474	474
$V_{O2} \rightarrow V_{O2}$	2.251	2.251	873	873
$V_{O3} \rightarrow V_{O3}$	1.766	1.766	685	685
$V_{O4} \rightarrow V_{O4}$	2.047	2.047	793	793
$V_{O1} \rightarrow V_{O2}$	2.154	1.501	835	582
$V_{O1} \rightarrow V_{O3}$	2.312	1.449	896	562

^aThe oxygen vacancy sites are defined in Figure 8, right panel.

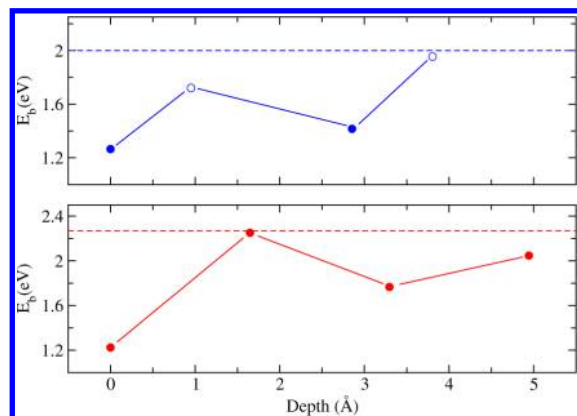


Figure 9. In-plane diffusion barrier E_b for the (10 $\bar{1}$ 0) (top panel) and (11 $\bar{2}$ 0) (bottom panel) surfaces as a function of the layer depth. The dashed lines correspond to the bulk limit (IN and OUT paths of Table 1 for the two surfaces, respectively).

to the (11 $\bar{2}$ 0) surface. In this specific case, a metastable state (local minimum) is found. The presence of such a minimum

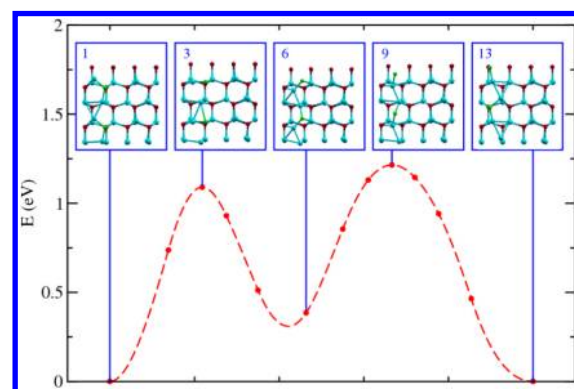


Figure 10. Potential energy profile of the $V_{O1} \rightarrow V_{O1}$ diffusion pathway. The insets show selected NEB images along the pathway. The oxygen atoms which undergo the larger displacements in the diffusion process are in green, while the zinc atoms and the other oxygen atoms are in blue and red, respectively.

has been further checked by optimizing a nearby structure (image 6) of the metastable state. The structure relaxed indeed to a configuration having 0.31 eV higher energy than the initial and final state of the pathway, confirming the reliability of the metastable state.

CONCLUSIONS

By using ab initio computational methods, we have investigated the formation and the diffusion of oxygen vacancies at the ZnO (10 $\bar{1}$ 0) and (11 $\bar{2}$ 0) surfaces. As expected, the formation energy tends to increase, when the vacancy moves from the surface to subsurface layer, approaching the bulk limit for sufficiently deep vacancy sites.

The study of the defected slab formation energy as a function of the oxygen chemical potential (that, in turn, depends on the external environment conditions) shows the possibility of obtaining, under strongly reducing conditions, reduced surfaces by varying the oxygen gas temperature and/or pressure. This is confirmed by a number of experiments, which were able also to measure the effects on the electronic and transport properties of the defects. Yet, at variance with other materials, such as TiO₂, obtaining stable defected surfaces is only achievable under well-defined experimental conditions, which explains why more recent STM studies do exclude the presence of oxygen vacancies at the surface. By comparing the energetics of three kinds of defects (O, Zn, and ZnO vacancies), we can also conclude that, differently from the O vacancy, there are no pressure and temperature conditions under which the Zn and ZnO vacancy defects get more stable than the stoichiometric surface.

The defect formation affects the surface electronic structure, in that an intragap occupied state shows up, with a “localized” character around the oxygen vacancy. The energy of the intragap state depends on the oxygen vacancy depth inside the material. Moreover, other fundamental properties, such as the surface gap energy and electron affinity, can be significantly altered by the presence of the defect and strongly depend on its position with respect to the surface.

Finally, we have also performed a detailed first-principles study of the diffusion behavior of oxygen vacancies both in the bulk ZnO crystal and in the ZnO (10 $\bar{1}$ 0) and (11 $\bar{2}$ 0) surfaces. We have found that the oxygen vacancies diffuse much more easily in the surface layer than in the bulk. In particular, we have verified that the surface diffusion can be activated at relatively modest temperature (490 K and 481 K for the (10 $\bar{1}$ 0) and (11 $\bar{2}$ 0) surfaces, respectively). Moreover, migration paths in the direction orthogonal to the surface show asymmetric barriers, which are smaller (by 0.5–0.9 eV) in the direction toward the surface, thus showing that the diffusion from subsurface layers to the surface is favored. Of course, it is expected that surface defects will remain stable only in the absence of O₂ since the surface vacancy sites are expected to be very reactive even at low temperatures.¹

AUTHOR INFORMATION

Corresponding Author

*E-mail: giovanni.cantele@spin.cnr.it.

Notes

The authors declare no competing financial interest.

ACKNOWLEDGMENTS

Financial support from the European Union Seventh Framework Program (FP7/2007-2013) under grant agreement N. 264098–MAMA is acknowledged.

REFERENCES

- (1) Göpel, W.; Lampe, U. *Phys. Rev. B* **1980**, *22*, 6447–6462.
- (2) Yamazoe, N. *Sens. Actuators, B* **1991**, *5*, 7–19.
- (3) Sberveglieri, G. *Sens. Actuators, B* **1995**, *23*, 103–109.
- (4) Azad, A. M.; Akbar, S. A.; Mhaisalkar, S. G.; Birkefeld, L. D.; Goto, K. S. *J. Electrochem. Soc.* **1992**, *139*, 3690–3704.
- (5) Choi, K. J.; Jang, H. W. *Sensors* **2010**, *10*, 4083–4099.
- (6) Korotcenkov, G. *Mater. Sci. Eng., B* **2007**, *139*, 1–23.
- (7) Barsan, N.; Kozielj, D.; Weimar, U. *Sens. Actuators, B* **2007**, *121*, 18–35.
- (8) Moos, R.; Sahnner, K.; Fleischer, M.; Guth, U.; Barsan, N.; Weimar, U. *Sensors* **2009**, *9*, 4323–4365.
- (9) Wang, C.; Yin, L.; Zhang, L.; Xiang, D.; Gao, R. *Sensors* **2010**, *10*, 2088–2106.
- (10) Batzill, M. *Sensors* **2006**, *6*, 1345–1366.
- (11) Batzill, M.; Katsiev, K.; Burst, J. M.; Diebold, U.; Chaka, A. M.; Delley, B. *Phys. Rev. B* **2005**, *72*, 165414.
- (12) Batzill, M.; Diebold, U. *Prog. Surf. Sci.* **2005**, *79*, 47–154.
- (13) Koshizaki, N.; Oyama, T. *Sens. Actuators, B* **2000**, *66*, 119–121.
- (14) Trani, F.; Causà, M.; Ninno, D.; Cantele, G.; Barone, V. *Phys. Rev. B* **2008**, *77*, 245410.
- (15) Chen, X.; Mao, S. S. *Chem. Rev.* **2007**, *107*, 2891–2959.
- (16) (a) Iacomino, A.; Cantele, G.; Ninno, D.; Marri, I.; Ossicini, S. *Phys. Rev. B* **2008**, *78*, 075405. (b) Iacomino, A.; Cantele, G.; Trani, F.; Ninno, D. *J. Phys. Chem. C* **2010**, *114*, 12389–12400. (c) Hameeuw, K.; Cantele, G.; Ninno, D.; Trani, F.; Iadonisi, G. *Phys. Status Solidi A* **2006**, *203*, 2219–2222.
- (17) Viswanath, R.; Ramasamy, S.; Ramamoorthy, R.; Jayavel, P.; Nagarajan, T. *Nanostr. Mater.* **1995**, *6*, 993–996.
- (18) Wu, M.; Azuma, A.; Shiosaki, T.; Kawabata, A. *IEEE Trans. Ultrasonics Ferroelectr. Freq. Control* **1989**, *36*, 442–445.
- (19) Jayaraj, M.; Antony, A.; Ramachandran, M. *Bull. Mater. Sci.* **2002**, *25*, 227–230.
- (20) Keis, K.; Bauer, C.; Boschloo, G.; Hagfeldt, A.; Westermarck, K.; Rensmo, H.; Siegbahn, H. *J. Photochem. Photobiol. A* **2002**, *148*, 57–64.
- (21) Yang, P.; Yan, H.; Mao, S.; Russo, R.; Johnson, J.; Saykally, R.; Morris, N.; Pham, J.; He, R.; Choi, H.-J. *Adv. Funct. Mater.* **2002**, *12*, 323–331.
- (22) (a) Hu, Y.; Lin, L.; Zhang, Y.; Wang, Z. L. *Adv. Mater.* **2012**, *24*, 110–114. (b) Hu, Y.; Zhang, Y.; Xu, C.; Lin, L.; Snyder, R. L.; Wang, Z. L. *Nano Lett.* **2011**, *11*, 2572–2577.
- (23) Roy, S.; Basu, S. *Bull. Mater. Sci.* **2002**, *25*, 513–515.
- (24) Raju, A.; Rao, C. *Sens. Actuators, B* **1991**, *3*, 305–310.
- (25) Patolsky, F.; Timko, B. P.; Zheng, G.; Lieber, C. M. *MRS Bull.* **2007**, *32*, 142–149.
- (26) Pan, Z. W.; Dai, Z. R.; Wang, Z. L. *Science* **2001**, *291*, 1947–1949.
- (27) McCluskey, M. D.; Jokela, S. J. *J. Appl. Phys.* **2009**, *106*, 071101.
- (28) Dutta, S.; Chattopadhyay, S.; Sarkar, A.; Chakrabarti, M.; Sanyal, D.; Jana, D. *Prog. Mater. Sci.* **2009**, *54*, 89–136.
- (29) Gupta, T. K.; Carlson, W. G. *J. Mater. Sci.* **1985**, *20*, 3487–3500.
- (30) Ramanachalam, M. S.; Rohatgi, A.; Schaffer, J. P.; Gupta, T. K. *J. Appl. Phys.* **1991**, *69*, 8380–8386.
- (31) Brillson, L. J.; Lu, Y. *J. Appl. Phys.* **2011**, *109*, 121301 and references therein.
- (32) Kohan, A. F.; Ceder, G.; Morgan, D.; Van de Walle, C. G. *Phys. Rev. B* **2000**, *61*, 15019–15027.
- (33) Zhang, S. B.; Wei, S.-H.; Zunger, A. *Phys. Rev. B* **2001**, *63*, 075205.
- (34) Oba, F.; Nishitani, S. R.; Isotani, S.; Adachi, H.; Tanaka, I. *J. Appl. Phys.* **2001**, *90*, 824–828.
- (35) Erhart, P.; Klein, A.; Albe, K. *Phys. Rev. B* **2005**, *72*, 085213.
- (36) Yan, Y.; Zhang, S. B.; Pantelides, S. T. *Phys. Rev. Lett.* **2001**, *86*, 5723–5726.
- (37) Limpijumnong, S.; Zhang, S. B.; Wei, S.-H.; Park, C. H. *Phys. Rev. Lett.* **2004**, *92*, 155504.
- (38) Pacchioni, G. *ChemPhysChem* **2003**, *4*, 1041–1047.
- (39) Erhart, P.; Albe, K. *Phys. Rev. B* **2006**, *73*, 115207.
- (40) Janotti, A.; Van de Walle, C. G. *Phys. Rev. B* **2007**, *76*, 165202.
- (41) Huang, G.-Y.; Wang, C.-Y.; Wang, J.-T. *J. Phys.: Condens. Matter* **2009**, *21*, 345802.
- (42) Kováčik, R.; Meyer, B.; Marx, D. *Angew. Chem., Int. Ed.* **2007**, *46*, 4894–4897.
- (43) Wang, Q.; Sun, Q.; Chen, G.; Kawazoe, Y.; Jena, P. *Phys. Rev. B* **2008**, *77*, 205411.
- (44) Göpel, W.; Brillson, L. J.; Brucker, C. F. *J. Vac. Sci. Technol.* **1980**, *17*, 894–898.
- (45) Diebold, U.; Koplitz, L. V.; Dulub, O. *Appl. Surf. Sci.* **2004**, *237*, 336–342.
- (46) Shao, X.; Fukui, K.-I.; Kondoh, H.; Shionoya, M.; Iwasawa, Y. *J. Phys. Chem. C* **2009**, *113*, 14356–14362.
- (47) Giannozzi, P.; Baroni, S.; Bonini, N.; Calandra, M.; Car, R.; Cavazzoni, C.; Ceresoli, D.; Chiarotti, G. L.; Cococcioni, M.; Dabo, I.; et al. *J. Phys.: Condens. Matter* **2009**, *21*, 395502.
- (48) Perdew, J. P.; Burke, K.; Ernzerhof, M. *Phys. Rev. Lett.* **1996**, *77*, 3865–3868.
- (49) Vanderbilt, D. *Phys. Rev. B* **1990**, *41*, 7892–7895.
- (50) We used the pseudopotentials O.pbe-van_ak.UPF and Zn.pbe-van.UPF from <http://www.quantum-espresso.org>.
- (51) Mordecai, A. *Nonlinear Programming: Analysis and Methods*; Dover: New York, 2003.
- (52) The BZ sampling meshes for all the other systems under investigation are scaled so as to be consistent, as close as possible, with that used for the bulk unit cell.
- (53) Birch, F. *J. Geophys. Res.* **1978**, *83*, 1257.
- (54) Calzolari, A.; Ruini, A.; Catellani, A. *J. Am. Chem. Soc.* **2011**, *133*, 5893–5899.

- (55) Decremps, F.; Datchi, F.; Saitta, A. M.; Polian, A.; Pascarelli, S.; Di Cicco, A.; Itié, J. P.; Baudelet, F. *Phys. Rev. B* **2003**, *68*, 104101.
- (56) Ozgur, U.; Alivov, Y. I.; Liu, C.; Teke, A.; Reshchikov, M. A.; Dogan, S.; Avrutin, V.; Cho, S.-J.; Morkoc, H. *J. Appl. Phys.* **2005**, *98*, 041301.
- (57) This slab thickness proved to be sufficient to ensure good convergence of the calculated properties when the point defect is moved towards the bulk-like (deeper) positions.
- (58) Cooke, D. J.; Marmier, A.; Parker, S. C. *J. Phys. Chem. B* **2006**, *110*, 7985–7991.
- (59) Hameeuw, K. J.; Cantele, G.; Ninno, D.; Trani, F.; Iadonisi, G. *J. Chem. Phys.* **2006**, *124*, 024708.
- (60) Bengtsson, L. *Phys. Rev. B* **1999**, *59*, 12301–12304.
- (61) Kaxiras, E.; Bar-Yam, Y.; Joannopoulos, J. D.; Pandey, K. C. *Phys. Rev. B* **1987**, *35*, 9625–9635.
- (62) Qian, G.-X.; Martin, R. M.; Chadi, D. J. *Phys. Rev. B* **1988**, *38*, 7649–7663.
- (63) Northrup, J. E. *Phys. Rev. Lett.* **1989**, *62*, 2487–2490.
- (64) Reuter, K.; Scheffler, M. *Phys. Rev. B* **2001**, *65*, 035406.
- (65) Linstrom, P. J.; Mallard, W. G. *NIST Chemistry WebBook, NIST Standard Reference Database Number 69*; National Institute of Standards and Technology: Gaithersburg MD, 20899, 2003.
- (66) Kulik, H. J.; Cococcioni, M.; Scherlis, D. A.; Marzari, N. *Phys. Rev. Lett.* **2006**, *97*, 103001.
- (67) Franchini, C.; Podloucky, R.; Paier, J.; Marsman, M.; Kresse, G. *Phys. Rev. B* **2007**, *75*, 195128.
- (68) Vineyard, G. H. *J. Phys. Chem. Solids* **1957**, *3*, 121–127.
- (69) (a) Henkelman, G.; Jóhannesson, G.; Jónsson, H. *Prog. Theor. Chem. Phys.* **2000**, *269*. (b) Henkelman, G.; Uberuaga, B. P.; Jónsson, H. *J. Chem. Phys.* **2000**, *113*, 9901–9904.
- (70) Duke, C. B.; Meyer, R. J.; Paton, A.; Mark, P. *Phys. Rev. B* **1978**, *18*, 4225–4240.
- (71) Dulub, O.; Boatner, L. A.; Diebold, U. *Surf. Sci.* **2002**, *519*, 201–217.
- (72) Meyer, B.; Marx, D. *Phys. Rev. B* **2003**, *67*, 035403 and references therein.
- (73) Spencer, M. J.; Wong, K. W.; Yarovsky, I. *Mater. Chem. Phys.* **2010**, *119*, 505–514.
- (74) Marana, N. L.; Longo, V. M.; Longo, E.; Martins, J. B. L.; Sambrano, J. R. *J. Phys. Chem. A* **2008**, *112*, 8958–8963.
- (75) Yan, Y.; Al-Jassim, M. M.; Wei, S.-H. *Phys. Rev. B* **2005**, *72*, 161307.
- (76) Calzolari, A.; Catellani, A. *J. Phys. Chem. C* **2009**, *113*, 2896–2902.
- (77) Kaewmaraya, T.; Pathak, B.; Araujo, C. M.; Rosa, A. L.; Ahuja, R. *Europhys. Lett.* **2012**, *97*, 17014.
- (78) Borriello, L.; Cantele, G.; Ninno, D.; Iadonisi, G.; Cossi, M.; Barone, V. *Phys. Rev. B* **2007**, *76*, 035430.
- (79) Clark, S. J.; Robertson, J.; Lany, S.; Zunger, A. *Phys. Rev. B* **2010**, *81*, 115311.
- (80) Meyer, B. *Phys. Rev. B* **2004**, *69*, 045416.
- (81) If we use instead the total energy of the O_2 molecule as obtained from the experimental measurements of E_f^{ZnO} , the stability of the defected surface at the lowest considered vacancy concentration occurs at ~ 1250 K.
- (82) As previously observed, if we use instead the total energy of the O_2 molecule as obtained from the experimental measurements of E_f^{ZnO} , the shift of the thermodynamic plots to high temperature is such that, in the O-rich limit (low-temperature limit), the Zn vacancy can become stable in a small temperature range,⁴² up to ~ 250 K in the example of Figure 6.
- (83) Huang, G.-Y.; Wang, C.-Y.; Wang, J.-T. *Solid State Commun.* **2009**, *149*, 199–204.
- (84) Erhart, P.; Albe, K. *Appl. Phys. Lett.* **2006**, *88*, 201918.
- (85) Gui-Yang, H.; Chong-Yu, W.; Jian-Tao, W. *Chin. Phys. B* **2010**, *19*, 013101.
- (86) (a) Vlasenko, L. S.; Watkins, G. D. *Phys. Rev. B* **2005**, *72*, 035203. (b) Vlasenko, L. S.; Watkins, G. D. *Phys. Rev. B* **2005**, *71*, 125210.